

# Statistically Equivalent Representative Volume Elements for Unidirectional Composite Microstructures: Part II – With Interfacial Debonding

SHRIRAM SWAMINATHAN AND SOMNATH GHOSH\*  
*Department of Mechanical Engineering, The Ohio State University  
650 Ackerman Road, Columbus, OH 43202*

(Received ...)

**ABSTRACT:** In this sequel to the study on microstructures without damage, methods for evaluating the statistically equivalent representative volume element (SERVE) are proposed for fiber-reinforced microstructures undergoing initiation and propagation of damage in the form of interfacial debonding. The microstructural analysis is executed using the Voronoi cell finite element model (VCFEM) in which the interface is modeled using a bilinear cohesive zone law. As introduced in the first article, a combination of statistical and computational tools is proposed to capture the evolving nature of the SERVE with increased loading. The effectiveness of alternative definitions and methods of characterizing the damaging microstructure is examined through numerical simulations.

**KEY WORDS:** statistically equivalent representative volume element (SERVE), Voronoi cell FEM (VCFEM), correlation functions, interfacial debonding.

## INTRODUCTION

**M**ICROSTRUCTURAL HETEROGENEITIES SUCH as fibers and particles in composite materials make them susceptible to increased damage and accelerated failure of the material. Dominant damage modes in the microstructure include fiber or particle cracking, fiber-matrix interfacial debonding, and brittle and ductile fracture in the matrix that can bridge discrete damage to propagate dominant cracks causing composite failure. In nonuniform microstructures, the initiation and propagation of damage are often influenced by the morphological features like inclusion size, spacing, directionality, clustering etc. as shown in [1]. As described in [2], the evaluation of the statistically

---

\*Author to whom correspondence should be addressed. E-mail: ghosh.5@osu.edu

equivalent representative volume element or SERVE for microstructures is of significant interest for the analysis of composite materials. For example, it is essential to incorporate the micromechanical analysis of the SERVE to develop the Continuum Damage Mechanics or CDM models for composites [3–7], which provides a framework for incorporating the effects of damage induced stiffness softening in constitutive equations using tensor forms of damage variables. Estimation of the SERVE for microstructures with evolving damage is a more extensive exercise in comparison with microstructures with no damage. Geometric parameters play a less significant role since the evolution of stresses and strains are affected by the dispersion of the evolving damage in the microstructure as well. Even when the microstructure is geometrically uniform, the initiation and progression of damage can result in a SERVE that is considerably larger than a unit cell.

In continuation with the first part of the study [2], the objective of this sequel article is to propose a methodology using similar statistical functions to evaluate SERVE for composite microstructures undergoing damage, characterized by interfacial debonding. The same statistical function and convergence based approach is used in the estimation of the size of SERVE that is postulated as the largest microregion that satisfies the following set of requirements:

- (i) Effective stress–strain behavior in the SERVE should be equivalent to the overall behavior of the material.
- (ii) Distribution functions of parameters reflecting the local morphology in the SERVE should be equivalent to those for the overall microstructure.
- (iii) The SERVE should be independent of the location in the local microstructure and the applied loading conditions.

The initiation and progression of damage in the microstructure requires the consideration of an evolving SERVE. The effectiveness of the metrics proposed in [2] for nonuniform microstructure is examined again with damage, and the difference between predictions for the undamaged and damaging microstructures are estimated. The article starts with an introduction to the Voronoi cell FEM that is used for micromechanical analysis of problems with interfacial debonding. Following this, the metrics that are used to estimate the SERVE are discussed. Finally, their effectiveness is assessed by application to a real microstructure of a fiber-reinforced unidirectional composite.

## THE VORONOI CELL FEM FOR MICROSTRUCTURES WITH DEBONDING

All micromechanical analysis in this study is done using the Voronoi Cell Finite Element Method (VCFEM) that has been developed by Ghosh et al. [1,8–10] for analyzing stresses and strains in heterogeneous microstructures of composite and porous materials. The VCFEM mesh naturally evolves from Dirichlet tessellation of non-uniform microstructural regions [11], with each element in VCFEM consisting of heterogeneity with its surrounding matrix. The method has been developed as an efficient tool for solving evolving microstructural problems such as particle cracking [9,10], and interfacial debonding [1,8]. In micromechanical problems of elastic composites with interfacial debonding, the VCFEM is coupled with cohesive zone

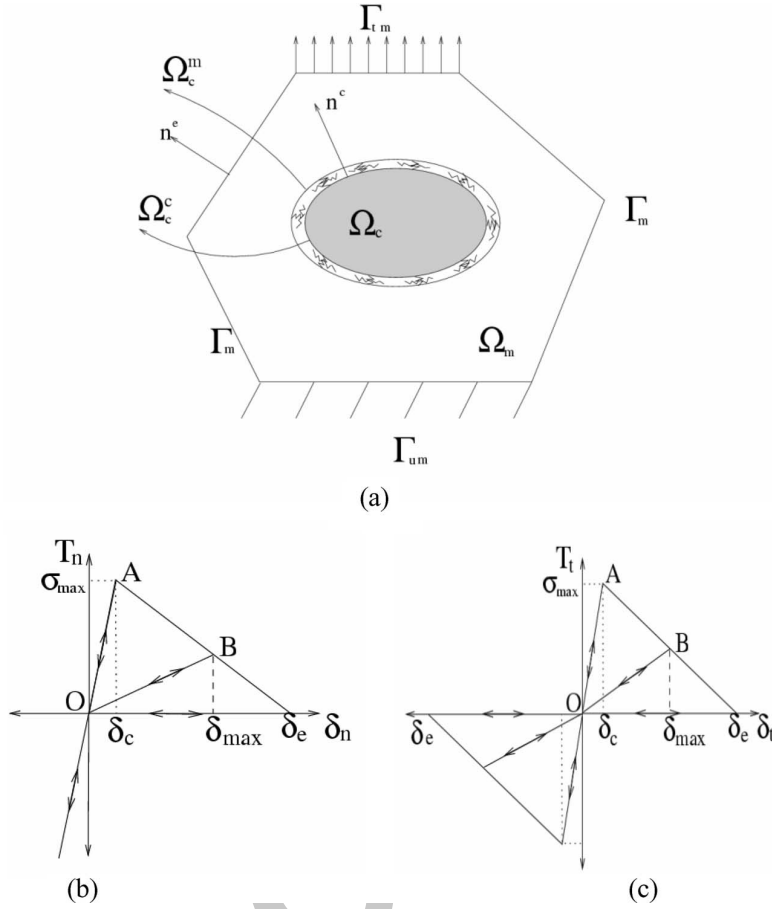


**Figure 1.** (a) Voronoi cell finite element with fiber-matrix interface modeled using nonlinear springs; (b) traction displacement relation ( $t_n - \delta_n$ ) for normal direction with  $\delta_t = 0$ ; and (c) traction displacement relation ( $t_t - \delta_t$ ) for tangential direction with  $\delta_n = 0$ .

models to depict debonding as a phenomenon of progressive separation across the interface that is resisted by cohesive tractions. A brief summary of the model developed in [8] is given below.

Consider a heterogeneous microstructural domain  $\Omega$  consisting of  $N$  inclusions each contained in a Voronoi cell element  $\Omega_e$ , as shown in Figure 1(a). The matrix and the inclusion phases are denoted by  $\Omega_m$  and  $\Omega_c$  such that  $\Omega_e = \Omega_m \cup \Omega_c$ . The element boundary  $\partial\Omega_e$  consists of prescribed traction boundary  $\Gamma_{tm}$ , prescribed displacement boundary  $\Gamma_{um}$  and the inter-element boundary  $\Gamma_m$ , i.e.,  $\partial\Omega_e = \Gamma_{tm} \cup \Gamma_{um} \cup \Gamma_m$ . An incompatible displacement field is facilitated across the interface through a set of connected node pairs to allow for de-cohesion of the matrix-inclusion interface. The nodes in each pair belong to the matrix and interface boundaries  $\partial\Omega_e^m$  and  $\partial\Omega_e^c$  respectively. The outward normal for  $\partial\Omega_e^c$  is given by  $n^c$  ( $=n^m$ ), while  $n^e$  is the outward normal for  $\partial\Omega_e^e$ . In the assumed stress hybrid formulation for VCFEM [8–10], the complimentary energy

functional for each element in terms of increments of stress and displacement is expressed as:

$$\begin{aligned}
\Pi_e(\boldsymbol{\sigma}, \Delta\boldsymbol{\sigma}, \mathbf{u}, \Delta\mathbf{u}) = & - \int_{\Omega_m} \Delta\mathbf{B}(\boldsymbol{\sigma}^m, \Delta\boldsymbol{\sigma}^m) d\Omega - \int_{\Omega_c} \Delta\mathbf{B}(\boldsymbol{\sigma}^c, \Delta\boldsymbol{\sigma}^c) d\Omega - \int_{\Omega_m} \boldsymbol{\varepsilon}^m : \Delta\boldsymbol{\sigma}^m d\Omega \\
& - \int_{\Omega_c} \boldsymbol{\varepsilon}^c : \Delta\boldsymbol{\sigma}^c d\Omega + \int_{\Omega_c} (\boldsymbol{\sigma}^m + \Delta\boldsymbol{\sigma}^m) \cdot \mathbf{n}^c \cdot (\mathbf{u}^m + \Delta\mathbf{u}^m) d\partial\Omega \\
& - \int_{\Gamma_{\text{im}}} (\bar{\mathbf{t}} + \Delta\bar{\mathbf{t}}) \cdot (\mathbf{u}^m + \Delta\mathbf{u}^m) d\Gamma \\
& + \int_{\partial\Omega_m^c} (\boldsymbol{\sigma}^m + \Delta\boldsymbol{\sigma}^m) \cdot \mathbf{n}^c \cdot (\mathbf{u}^m + \Delta\mathbf{u}^m) d\partial\Omega \\
& + \int_{\partial\Omega_c^c} (\boldsymbol{\sigma}^c + \Delta\boldsymbol{\sigma}^c) \cdot \mathbf{n}^c \cdot (\mathbf{u}^c + \Delta\mathbf{u}^c) d\partial\Omega \\
& - \int_{\partial\Omega_m^c/\partial\Omega_c^c} \int_{\mathbf{u}_n^m - \mathbf{u}_n^c}^{\mathbf{u}_n^m + \Delta\mathbf{u}_n^m - \mathbf{u}_n^c + \Delta\mathbf{u}_n^c} \mathbf{T}_n d(\mathbf{u}_n^m - \mathbf{u}_n^c) d\partial\Omega \\
& - \int_{\partial\Omega_m^c/\partial\Omega_c^c} \int_{\mathbf{u}_t^m - \mathbf{u}_t^c}^{\mathbf{u}_t^m + \Delta\mathbf{u}_t^m - \mathbf{u}_t^c + \Delta\mathbf{u}_t^c} \mathbf{T}_t d(\mathbf{u}_t^m - \mathbf{u}_t^c) d\partial\Omega
\end{aligned} \tag{1}$$

Here  $\mathbf{B}$  is the complementary energy density and the superscripts m and c correspond to variables associated with the matrix and inclusion phases respectively.  $\boldsymbol{\sigma}^m$  and  $\boldsymbol{\sigma}^c$  are the equilibrated stress fields,  $\boldsymbol{\varepsilon}^m$  and  $\boldsymbol{\varepsilon}^c$  the corresponding strain fields in the different phases of each Voronoi element. The kinematically admissible displacement fields on  $\partial\Omega_c$ ,  $\partial\Omega_m^c$ , and  $\partial\Omega_c^c$  are given by  $\mathbf{u}$ ,  $\mathbf{u}^m$ , and  $\mathbf{u}^c$  respectively. The prefix  $\Delta$  corresponds to increments. The last two terms provide the work done by the interfacial tractions  $\mathbf{T}^m = T_n^m \mathbf{n}^m + T_t^m \mathbf{t}^m$  due to interfacial separation  $(\mathbf{u}^m - \mathbf{u}^c)$ , where  $\mathbf{T}_n$  and  $\mathbf{T}_t$  are the normal and tangential components that are described by cohesive laws. The total energy for the entire heterogeneous domain is obtained by adding energy functionals for  $N$  elements as

$$\Pi = \sum_{e=1}^N \Pi_e \tag{2}$$

The details of the formulation and the solution methodology are given in Ghosh et al. [8]. Each node pair on the fiber–matrix interface is connected by nonlinear springs in the normal and tangential directions whose behavior is governed by cohesive laws. These laws relate the normal and tangential components of the interfacial tractions ( $T_n, T_t$ ) with that of the interfacial separations ( $\delta_n (= \mathbf{u}_n^m - \mathbf{u}_n^c)$ ,  $\delta_t (= \mathbf{u}_t^m - \mathbf{u}_t^c)$ ). The traction across the interface reaches a maximum, subsequently decreases and eventually vanishes with increasing displacement jump. A number of cohesive zone models have been proposed by various authors [12–16]. In this work, the bilinear cohesive zone model, postulated by Ortiz and Pandolfi [16] is used to represent interfacial debonding. The relation between the effective traction  $t (= \sqrt{T_n^2 + T_t^2})$  and the effective decohesion displacement  $\delta (= \sqrt{\delta_n^2 + \beta^2 \delta_t^2})$  in this model is expressed through a free energy potential  $\phi$  as

$$t = \frac{\partial\phi(\delta)}{\partial\delta} \tag{3}$$

with the factor  $\beta$  being introduced to provide different weights to normal and tangential displacements. The mathematical form of the  $t$ - $\delta$  relation in this model is expressed as

$$t = \begin{cases} \frac{\sigma_{\max}}{\delta_c} \delta & \text{if } \delta \leq \delta_c \text{ (hardening region)} \\ \frac{\sigma_{\max}}{\delta_c - \delta_e} (\delta - \delta_e) & \text{if } \delta_c < \delta \leq \delta_e \text{ (softening region)} \\ 0 & \text{if } \delta > \delta_e \text{ (complete debonding)} \end{cases} \quad (4)$$

The normal and tangential tractions are derived as

$$T_n = \frac{\partial \phi}{\partial \delta_n} = \frac{\partial \phi}{\partial \delta} \frac{\partial \delta}{\partial \delta_n} = \begin{cases} \frac{\sigma_{\max}}{\delta_c} \delta_n & \text{if } \delta \leq \delta_c \\ \frac{\sigma_{\max}}{\delta} \frac{\delta - \delta_e}{\delta_c - \delta_e} \delta_n & \text{if } \delta_c < \delta \leq \delta_e \\ 0 & \text{if } \delta > \delta_e \end{cases} \quad (5)$$

$$T_t = \frac{\partial \phi}{\partial \delta_t} = \frac{\partial \phi}{\partial \delta} \frac{\partial \delta}{\partial \delta_t} = \begin{cases} \frac{\sigma_{\max}}{\delta_c} \beta^2 \delta_t & \text{if } \delta \leq \delta_c \\ \frac{\sigma_{\max}}{\delta} \frac{\delta - \delta_e}{\delta_c - \delta_e} \beta^2 \delta_t & \text{if } \delta_c < \delta \leq \delta_e \\ 0 & \text{if } \delta > \delta_e \end{cases}$$

Figure 1(b) and (c) show the normal traction–separation response for  $\delta_t = 0$  and tangential traction–separation response for  $\delta_n = 0$  respectively. The unloading behavior in the hardening region (OA in Figure 1(b) and (c)) follows the same slope as that of the loading path. In the softening region, unloading is assumed to follow a different linear path back from the current position to the origin with a reduced stiffness (line BO in Figure 1(b) and (c)) and is expressed as

$$t = \frac{\sigma_{\max}}{\delta_{\max}} \frac{\delta_{\max} - \delta_e}{\delta_c - \delta_e} \delta \quad \delta_c < \delta_{\max} < \delta_e \quad \text{and} \quad \delta < \delta_{\max} \quad (6)$$

Reloading follows the hardening path OB and then continues along the softening slope, consistent with the irreversible nature of the damage process. Both the normal and tangential tractions vanish for  $\delta > \delta_e$ . A detailed discussion on the derivation of the cohesive parameter has been presented in [8].

### MEASURES OF ESTIMATING SERVE FOR MICROSTRUCTURES UNDERGOING DAMAGE

The evolving nature of the microstructure with initiation and propagation of damage requires a continuous rendering of the SERVE with changing loads. Various methods, some of them employing statistical functions, are used to extract the SERVE windows progressively. At any given stage of damage evolution, the largest microregion obtained from the alternative approaches can be regarded as the instantaneous size scale of the SERVE. Different measures used in the task are discussed here.

### Convergence of the Stiffness Tensor

For the damaged microstructure, the convergence of the degrading homogenized stiffness tensor  $[E_{ijkl}^H]$  is taken to be an indicator of the region of influence in the microstructure and hence as a metric for estimating the microstructural SERVE [2]. Instead of the tangent stiffness tensor, this is taken to be the linear unloading stiffness tensor from the point of loading in the macroscopic stress–strain plot as shown in Figure 2. In this evaluation process, the macroscopic stress  $\bar{\sigma}_{ij}$  is the volume averaged stress obtained by integrating the stress over the microstructural RVE [7,17] as

$$\bar{\sigma}_{ij} = \frac{1}{Y} \int_Y \sigma_{ij}(Y) dY \quad (7)$$

where  $Y$  is the microstructure RVE. The corresponding macroscopic strain  $\bar{\varepsilon}_{ij}$  is the volume averaged strain, expressed as

$$\bar{\varepsilon}_{ij} = \frac{1}{Y} \int_Y \varepsilon_{ij}(Y) dY = \frac{1}{Y} \left[ \int_{Y_m} \varepsilon_{ij}(Y) dY + \int_{Y_f} \varepsilon_{ij}(Y) dY + \int_{Y_{int}} \varepsilon_{ij}(Y) dY \right] \quad (8)$$

where  $Y_m$ ,  $Y_f$ , and  $Y_{int}$  correspond to the matrix, fiber and interface regions respectively. The interface  $Y_{int}$  is expressed as a region between the matrix and inclusion boundaries and consequently, the integral of strain over  $Y_{int}$  is expressed in terms of the jumps in the displacements across the interface by applying divergence theorem to the last term of Equation (8).

$$\bar{\varepsilon}_{ij} = \frac{1}{Y} \int_Y \varepsilon_{ij}(Y) dY + \frac{1}{2Y} \int_{\partial Y_{int}} ([u_i]n_j + [u_j]n_i) dS \quad (9)$$

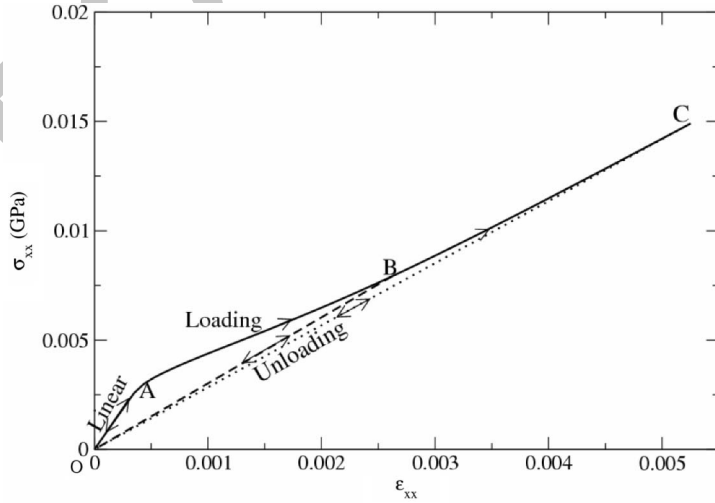


**Figure 2.** Macroscopic stress–strain curve for microstructure.

Here  $[u_i]$  denotes the jump of the displacement components across the interface with an outward normal  $n_i$ . For a unit cell with the matrix–fiber interface represented by the cohesive zone model of Figure 1, various regions in the macroscopic stress–strain diagram of Figure 2 can be correlated to regions of the cohesive zone model. For example, the linear region from O to A corresponds to the positive slope zone for  $\delta \leq \delta_c$ . The nonlinear region from A to C corresponds to the softening and consequent debonding zone for  $\delta > \delta_c$ . Unloading from any point in the nonlinear region, results in linear unloading paths like B–O or C–O in the stress–strain plot. For the point B, re-loading will cause the stress–strain behavior to follow the path O–B–C while for the point C, re-loading will follow the path O–C. For a given microstructural RVE, the stiffness tensor can be evaluated at any strain by computing the stiffness in unloading at that strain field. Individual components of the stiffness tensor are obtained as the solution to the three separate boundary value problems as outlined in [7,17]. These problems are characterized by periodic boundary conditions with imposed unit macroscopic strain fields, given by

$$\begin{cases} \bar{\epsilon}_{xx} \\ \bar{\epsilon}_{yy} \\ \bar{\epsilon}_{xy} \end{cases}^{\text{I}} = \begin{cases} 1 \\ 0 \\ 0 \end{cases}, \quad \begin{cases} \bar{\epsilon}_{xx} \\ \bar{\epsilon}_{yy} \\ \bar{\epsilon}_{xy} \end{cases}^{\text{II}} = \begin{cases} 0 \\ 1 \\ 0 \end{cases}, \quad \begin{cases} \bar{\epsilon}_{xx} \\ \bar{\epsilon}_{yy} \\ \bar{\epsilon}_{xy} \end{cases}^{\text{III}} = \begin{cases} 0 \\ 0 \\ 1 \end{cases} \quad (10)$$

The strain in the fiber direction is set as zero,  $\bar{\epsilon}_{zz} = 0$ . Following steps outlined in [5], the size scale of SERVE windows are estimated from the convergence characteristics of the stiffness tensor in unloading at different values of macroscopic strains.

### Marked Correlation Function in Terms of Damage Variables

The marked correlation function  $M(r)$  can be used again for estimating the SERVE in the presence of evolving damage, where a ‘mark’ is chosen as a characteristic damage variable that evolves with increasing strain. For each fiber, the mark assigned is the inverse of the magnitude of the tensile traction that is averaged over the length of the non-debonded or intact portion of interface. The traction in this case is evaluated as the resultant of the normal and tangential components given as  $\sqrt{T_n^2 + T_t^2}$ . Since the tractions are expected to increase with decreasing distances between inclusions, the inverse of the traction is taken as the mark to achieve a positive correlation between the marks and the distances. Only points that have tensile normal components at a fiber–matrix interface are considered for the traction calculation and points with compressive normal components are neglected. These traction values may lie either in the hardening or softening regions of the cohesive zone model. In the softening region, the tractions will decrease with increasing displacement jump and eventually reduce to zero, signaling the onset of microstructural damage due to interfacial debonding. With the propagation of debonding, tractions at the intact portion in the interface will tend to lie in the softening region of the cohesive zone model and will have values that are close to zero. Consequently, the average of the traction values in the intact portion of the interface will give a quantitative measure of the closeness to debonding and hence is represented by this mark. The marked correlation function  $M(r)$  is evaluated at different

values of macroscopic strains and the SERVE size is estimated at each strain level using steps outlined in the first part of this article [2].

### Distribution of Critical Microstructural Variables

The distribution of critical interfacial fraction or (CIF) is compared for the candidate RVEs and the entire microstructure to estimate the size of SERVE. In this case, the CIF is evaluated as the ratio of the interface length  $l_{ic}$ , which has a traction below a critical value  $T_c$ , to the total length of the interface  $l_{me}$  in the microstructural element. As explained in Section 3.2, the resultant traction is evaluated from the resultant of the normal and tangential components. Again, only the tensile normal components are considered for traction calculation and compressive tractions are neglected. These traction values are defined by the cohesive zone and will range from the peak stress to zero. From the CIF distribution, inferences can be made regarding the fraction of points on the verge of debonding and the general traction state at the fiber–matrix interfaces in the microstructure. With the onset of debonding, the value of CIF at zero traction gives the fraction of the total interface that has been damaged in the microstructure due to interfacial debonding. To test for convergence, CIF distributions for the candidate RVEs and for the entire microstructure, are compared. For the cohesive zone interface models, the CIF will be 100% for when  $T_c$  corresponds to the peak stress in the cohesive law, since this is the highest possible traction achievable. The CIF is estimated at various strain increments in the loading process, following steps outlined in [2]. The largest microstructural region, estimated by the method for all strains is estimated as the SERVE for the damaged microstructure.

## EVALUATION OF SERVE FOR A COMPOSITE MICROGRAPH

The  $100 \times 79.09 \mu\text{m}^2$  optical micrograph of a steel fiber-reinforced polymer matrix composite considered in [2] is once again examined with evolving damage in this study. The fibers are aligned perpendicular to the plane of the paper and have circular cross-sections with a radius of  $1.75 \mu\text{m}$ . A 2D plane strain assumption ( $\varepsilon_{zz} = 0, \varepsilon_{xz} = 0, \varepsilon_{yz} = 0$ ) is made in the micromechanical analysis of the composite problem, with the  $z$ -direction along the fiber. The matrix material is an epoxy with Young's modulus,  $E_m = 4.6 \text{ GPa}$  and Poisson's ratio,  $\nu_m = 0.4$ , while the fiber material is steel with Young's modulus,  $E_f = 210 \text{ GPa}$  and Poisson's ratio,  $\nu_f = 0.3$ . Parameters for the cohesive zone law for the interface are  $\sigma_{\max} = 0.0025 \text{ GPa}$ ,  $\delta_c = 5.1 \times 10^{-5}$ ,  $\delta_e = 6.2 \times 10^{-4}$  and  $\beta = 0.707$ . The micromechanical problems are solved for three different macroscopic strain conditions, subjected to periodic boundary conditions. These loading conditions are:

- (i) imposed macroscopic normal strain field

$$\begin{Bmatrix} \bar{\varepsilon}_{xx} \\ \bar{\varepsilon}_{yy} \\ \bar{\varepsilon}_{xy} \end{Bmatrix}^T = \begin{Bmatrix} 5.25e - 03 \\ 0 \\ 0 \end{Bmatrix};$$

(ii) imposed macroscopic normal strain field

$$\begin{Bmatrix} \bar{\varepsilon}_{xx} \\ \bar{\varepsilon}_{yy} \\ \bar{\varepsilon}_{xy} \end{Bmatrix}^{\text{II}} = \begin{Bmatrix} 0 \\ 5.25e - 03 \\ 0 \end{Bmatrix};$$

(iii) imposed macroscopic shear strain field

$$\begin{Bmatrix} \bar{\varepsilon}_{xx} \\ \bar{\varepsilon}_{yy} \\ \bar{\varepsilon}_{xy} \end{Bmatrix}^{\text{III}} = \begin{Bmatrix} 0 \\ 0 \\ 12.0e - 03 \end{Bmatrix}.$$

The strain levels are found to be sufficient for causing significant debonding at most fiber–matrix interfaces in the microstructure. The micromechanical analysis is conducted with the Voronoi cell FEM [8] with interfacial debonding. The imposed strains are applied in small and equal increments for the duration of the loading. The simulations are carried out in a standalone single processor SUN Workstation. The computational time for every 100 fiber simulations using VCFEM for each of the above loading conditions is  $\approx 12$  min per increment of the damage simulation. The methodologies described in the previous section are now applied to evaluate the size of the SERVE for the three loading conditions.

### Convergence of the Stiffness Tensor

Windows of increasing sizes ranging from  $\approx 22 \mu\text{m}$  window containing 20 fibers to  $63 \mu\text{m}$  window containing 150 fibers with periodic boundaries are analyzed using the procedure of constructing windows by periodic repetition of fibers explained in [2]. The area fractions of each of these windows are almost the same as that of the entire micrograph, as shown in Table 1 of [2]. The stiffness tensor in unloading for the microstructure as well as for the increasing window sizes are evaluated at the terminal values of the macroscopic strain

**Table 1. Comparison of the stiffness tensor computed from the micrograph and from the SERVE window for imposed macroscopic strain in x-direction.**

Stiffness tensor (GPA) with $\varepsilon_{xx} = 2.625e - 03$			Stiffness tensor (GPA) with $\varepsilon_{xx} = 5.25e - 03$		
Micrograph	SERVE (52 $\mu\text{m}$ )		Micrograph	SERVE (63 $\mu\text{m}$ )	
$\begin{pmatrix} 3.02 & 1.50 & -0.03 \\ 1.50 & 4.02 & -0.02 \\ -0.03 & -0.02 & 0.98 \end{pmatrix}$	$\begin{pmatrix} 3.04 & 1.53 & -0.03 \\ 1.53 & 4.07 & -0.02 \\ -0.03 & -0.02 & 0.99 \end{pmatrix}$	$\begin{pmatrix} 2.83 & 1.29 & -0.03 \\ 1.29 & 3.22 & -0.02 \\ -0.03 & -0.02 & 0.85 \end{pmatrix}$	$\begin{pmatrix} 2.83 & 1.28 & -0.03 \\ 1.28 & 3.21 & -0.02 \\ -0.03 & -0.02 & 0.85 \end{pmatrix}$		

mentioned above. Figures 3(a)–5(a) show the convergence of the components of the unloading stiffness tensor with increasing RVE size. The corresponding deviation from the values for the entire micrograph is depicted in Figures 3(b)–5(b). For all the three loading conditions, windows containing over 100 fibers show a difference of less than 5% from the stiffness components for the entire micrograph at the final strain. The window of size  $63\ \mu\text{m}$  containing 150 fibers shows a less than 2% deviation in all cases and is taken to be the SERVE at this strain level. The size of the SERVE changes with increasing damage in the microstructure as shown in Figure 6. For low strains, the SERVE is of size  $35\ \mu\text{m}$ , containing about 52 fibers for all the three strain conditions, as also depicted in [2]. However, the SERVE size increases at a much slower rate for the shear strain condition than for the normal strains. This is a consequence of the extent of damage with these respective strain conditions, which in turn is also a function of the

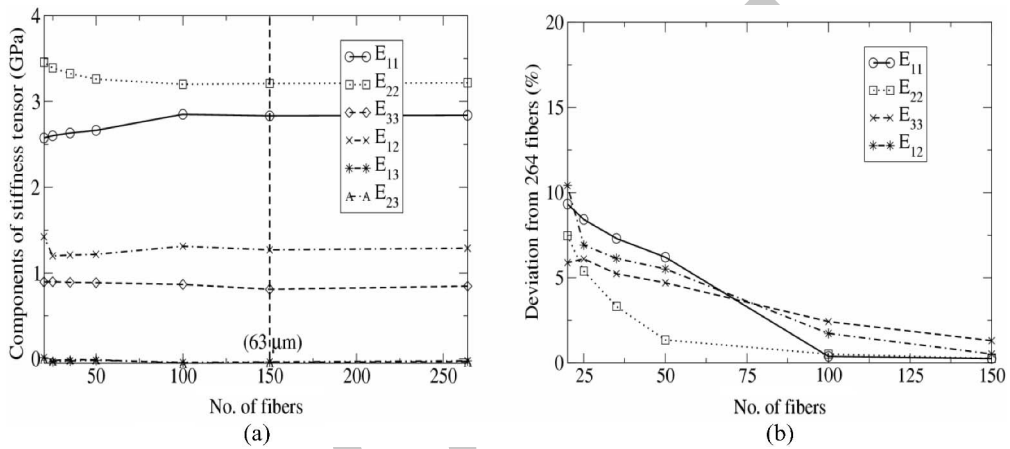


**Figure 3.** Plots showing (a) convergence of the stiffness tensor components for macroscopic  $\varepsilon_{xx} = 5.25e - 03$  and (b) deviation of the stiffness tensor from that of the micrograph.

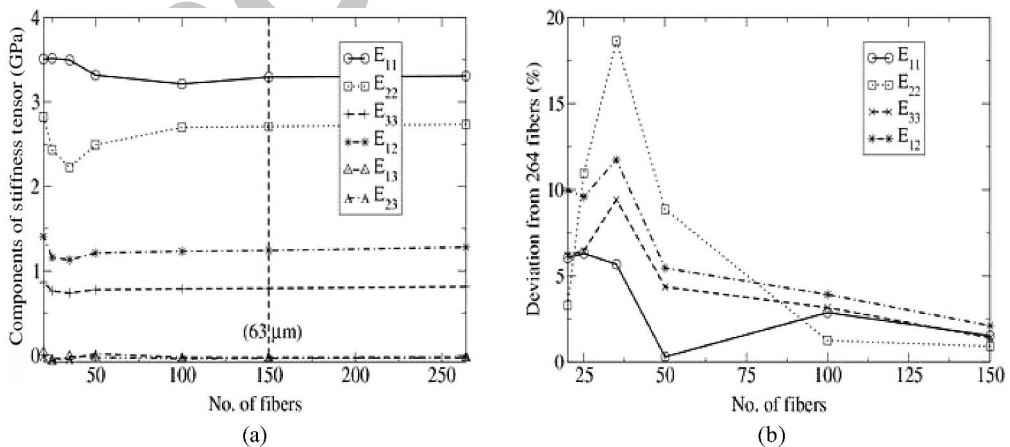


**Figure 4.** Plots showing (a) convergence of the stiffness tensor components for macroscopic  $\varepsilon_{yy} = 5.25e - 03$  and (b) deviation of the stiffness tensor from that of the micrograph.

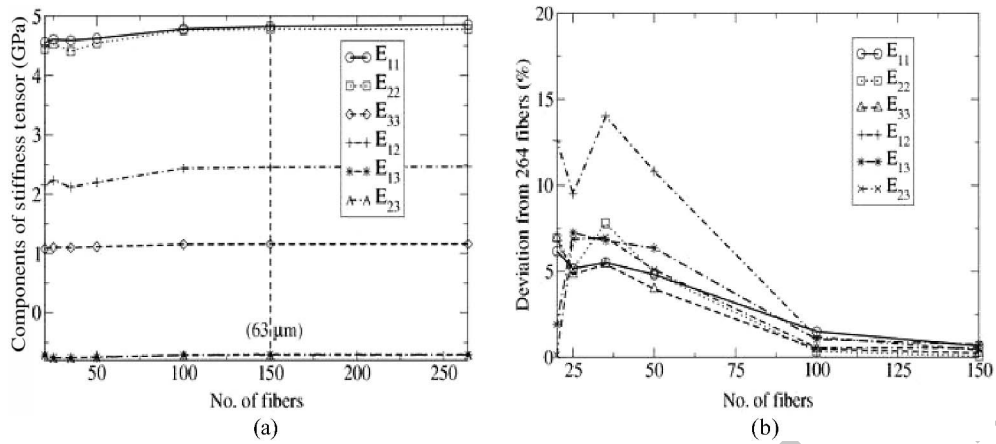


**Figure 5.** Plots showing (a) convergence of the stiffness tensor components for macroscopic  $\varepsilon_{xy} = 12e - 03$  and (b) deviation of the stiffness tensor from that of the micrograph.

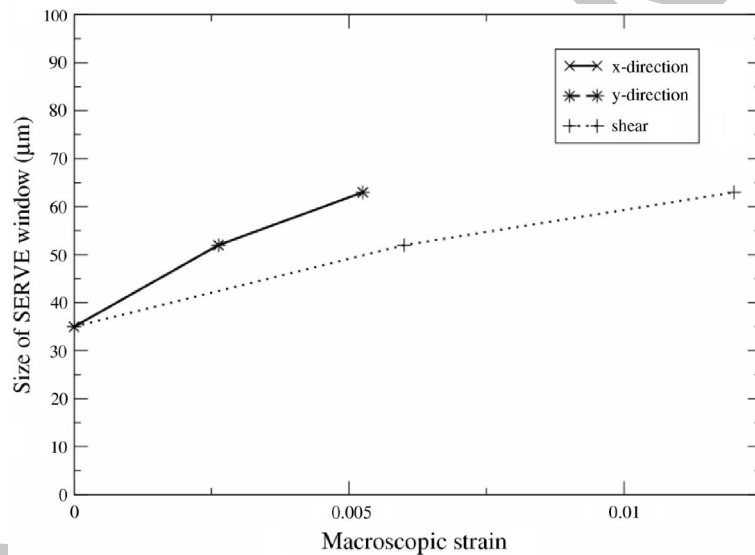


**Figure 6.** SERVE size for imposed macroscopic strains in normal directions and shear from convergence of the stiffness tensor in unloading.

interface integrity and hence the cohesive law parameters. The initial undamaged stiffness of the micrograph is:

$$[E_{ij}]^H = \begin{pmatrix} 16.44 & 9.59 & -0.03 \\ 9.59 & 16.30 & -0.02 \\ -0.03 & -0.02 & 3.50 \end{pmatrix}$$

**Table 2. Comparison of the stiffness tensor computed from the micrograph and from the SERVE window for imposed macroscopic strain in y-direction.**

Stiffness tensor (GPA) with $\varepsilon_{yy} = 2.625e-03$			Stiffness tensor (GPA) with $\varepsilon_{yy} = 5.25e-03$		
Micrograph	SERVE (52 $\mu\text{m}$ )	Micrograph	SERVE (63 $\mu\text{m}$ )	Micrograph	SERVE (63 $\mu\text{m}$ )
$\begin{pmatrix} 4.05 & 1.48 & -0.03 \\ 1.48 & 2.91 & -0.02 \\ -0.03 & -0.02 & 0.90 \end{pmatrix}$	$\begin{pmatrix} 3.96 & 1.44 & -0.03 \\ 1.44 & 2.91 & -0.02 \\ -0.03 & -0.02 & 0.90 \end{pmatrix}$	$\begin{pmatrix} 3.31 & 1.28 & -0.03 \\ 1.28 & 2.73 & -0.02 \\ -0.03 & -0.02 & 0.81 \end{pmatrix}$	$\begin{pmatrix} 3.23 & 1.25 & -0.03 \\ 1.25 & 2.71 & -0.02 \\ -0.03 & -0.02 & 0.79 \end{pmatrix}$	$\begin{pmatrix} 3.31 & 1.28 & -0.03 \\ 1.28 & 2.73 & -0.02 \\ -0.03 & -0.02 & 0.81 \end{pmatrix}$	$\begin{pmatrix} 3.23 & 1.25 & -0.03 \\ 1.25 & 2.71 & -0.02 \\ -0.03 & -0.02 & 0.79 \end{pmatrix}$

**Table 3. Comparison of the stiffness tensor computed from the micrograph and from the SERVE window for imposed macroscopic shear.**

Stiffness tensor (GPA) with $\varepsilon_{xy} = 6.0e-03$			Stiffness tensor (GPA) with $\varepsilon_{xy} = 12.0e-03$		
Micrograph	SERVE (52 $\mu\text{m}$ )	Micrograph	SERVE (63 $\mu\text{m}$ )	Micrograph	SERVE (63 $\mu\text{m}$ )
$\begin{pmatrix} 5.01 & 2.51 & -0.67 \\ 2.51 & 4.94 & -0.68 \\ -0.67 & -0.68 & 1.20 \end{pmatrix}$	$\begin{pmatrix} 4.95 & 2.48 & -0.68 \\ 2.48 & 4.93 & -0.68 \\ -0.68 & -0.68 & 1.19 \end{pmatrix}$	$\begin{pmatrix} 4.86 & 2.47 & -0.71 \\ 2.47 & 4.78 & -0.71 \\ -0.71 & -0.71 & 1.16 \end{pmatrix}$	$\begin{pmatrix} 4.83 & 2.44 & -0.71 \\ 2.44 & 4.78 & -0.71 \\ -0.71 & -0.71 & 1.15 \end{pmatrix}$	$\begin{pmatrix} 4.86 & 2.47 & -0.71 \\ 2.47 & 4.78 & -0.71 \\ -0.71 & -0.71 & 1.16 \end{pmatrix}$	$\begin{pmatrix} 4.83 & 2.44 & -0.71 \\ 2.44 & 4.78 & -0.71 \\ -0.71 & -0.71 & 1.15 \end{pmatrix}$

It is observed that within the prescribed tolerance, the stiffness tensor of the micrograph indicates isotropy. Tables 1–3 show the degradation of the stiffness tensor with the evolution of the SERVE window for the three strain conditions. From Tables 1–3, it is observed that the components  $E_{11}$  and  $E_{22}$  differ significantly from one another with the evolution of damage in the microstructure. In Table 3, the components  $E_{13}$ ,  $E_{23}$ ,  $E_{31}$ , and  $E_{32}$  exhibit increased nonzero values and the component  $E_{33}$  reduces with the evolution of microstructural damage. Hence, for all the three loading cases with evolving damage, the initially isotropic microstructure degrades into an anisotropic microstructure. It should be noted that due to the relative small size of the micrograph with respect to the SERVE size, the SERVE is not totally independent of the location in the micrograph and the maximum size is represented in the figures.

### SERVE from Marked Correlation Functions

The marked correlation function  $M(r)$  is evaluated for the micrograph at different strain intervals with the marks chosen as the inverse of averaged traction over the intact interface. The plots of the  $M(r)$  for the terminal values of the applied macroscopic strains in the normal directions and shear are depicted in Figure 7. Convergence of  $M(r)$  is assumed if the percentage increase of incremental area under each  $M(r)$  curve is below a pre-determined tolerance (5% in this study). From Figure 7, it is observed that all the three  $M(r)$  plots converge with unity ( $M(r) = 1$ ) at a radius of convergence  $r_p$  of  $\sim 31 \mu\text{m}$ , containing about 145 fibers. The radius of convergence  $r_p$  monotonically increases with damage evolution in the microstructure as shown in Figure 8. The SERVE size at the terminal strain is  $\sim 62 \mu\text{m}$ , almost 1.7 times higher than for the undamaged interface  $\sim 36 \mu\text{m}$ . As in the previous consideration, the rate of increase in SERVE size is found to be similar

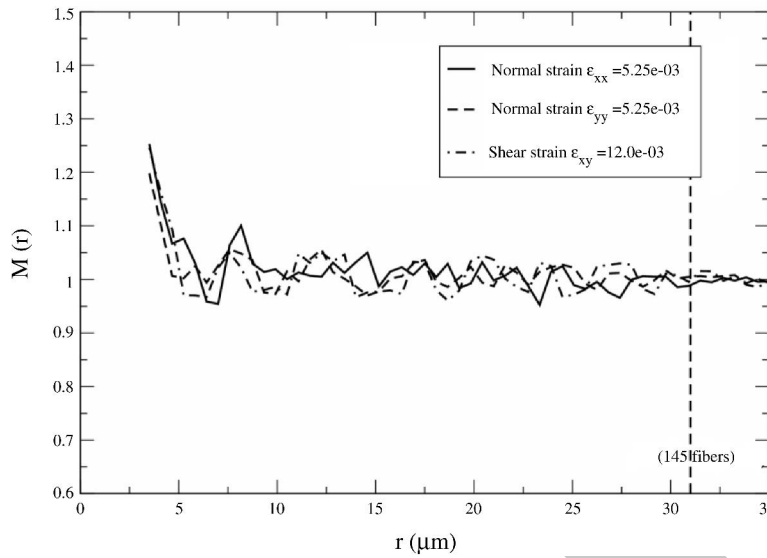


Figure 7. Plots of  $M(r)$  for applied macroscopic strains in normal directions and shear for inverse of averaged traction acting over intact interface.

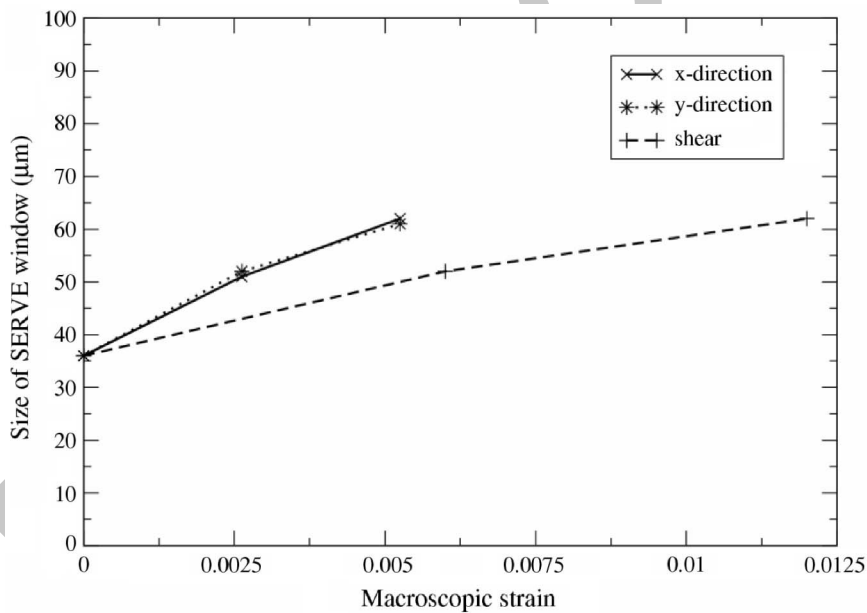
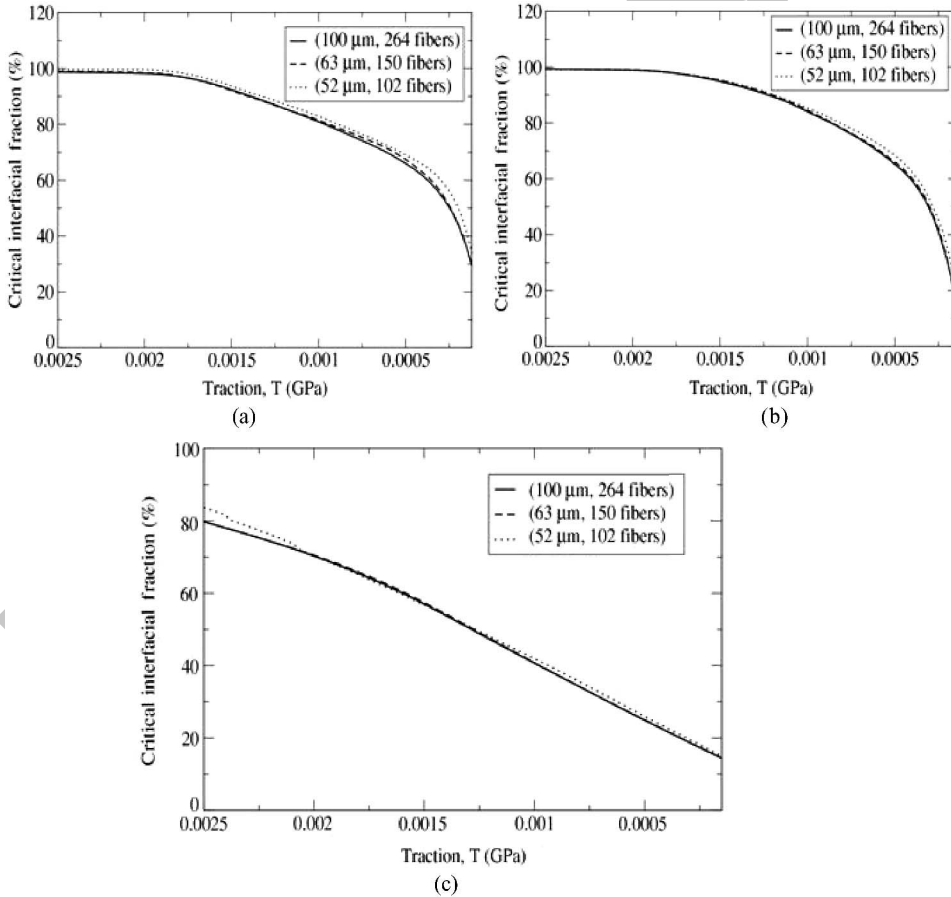


Figure 8. SERVE size for imposed macroscopic strains in normal directions and shear from  $M(r)$  function.

for the applied normal strains, but is slower for shear strain. Also, Figure 7 shows that the values of  $M(r)$  for the three loading cases significantly differ from one another until the convergence radius  $r_p$  is reached. This is attributed to the directional dependence of the marked values with the applied loading directions until the radius  $r_p$ , which is more pronounced for a damaged microstructure compared to undamaged ones.

### SERVE from Distribution of Critical Microstructural Variables

Following steps summarized in the section ‘Distribution of Critical Microstructural Variables’, windows of increasing sizes with periodic boundaries are subjected to the loading conditions mentioned above. The distributions of the CIF for the micrograph and windows of various sizes are evaluated at various strain intervals and plotted. Figure 9(a)–(c) show the plots for the terminal values of the applied strains. The maximum value of the critical traction  $T_c$  corresponds to the peak stress,  $\sigma_{\max}$  ( $= 0.0025$  GPa) in the cohesive law while the minimum value of  $T_c$  corresponds to 0 for a fully debonded interface. For the imposed macroscopic strain  $\epsilon_{xx}$ ,  $\approx 30\%$  of the total interface in the micrograph is found to have been debonded, while the corresponding percentages for  $\epsilon_{yy}$  and  $\epsilon_{xy}$  are  $\sim 18\%$  and  $15\%$  respectively. Additionally, in the case of imposed shear strain, it is seen that about 20% of the total interface in the micrograph experiences compressive normal tractions.



**Figure 9.** Critical interfacial fraction ( $T \leq T_c$ ) as a function of the interfacial traction for (a) macroscopic strain  $\epsilon_{xx} = 5.25e - 03$ ; (b) macroscopic strain  $\epsilon_{yy} = 5.25e - 03$ ; and (c) macroscopic strain  $\epsilon_{xy} = 12e - 03$ .

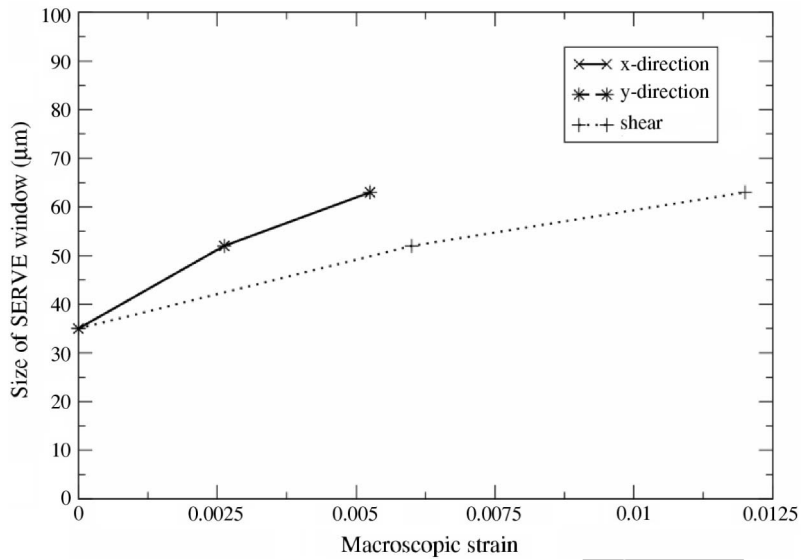


**Figure 10.** SERVE size for imposed macroscopic strains in *x* and *y* directions and shear from critical Interfacial fraction distribution.

From the Figure 9(a)–(c), it is observed that windows containing 150 fibers show a deviation of less than 3% in the CIF plots when compared with the entire micrograph. The percentage of damaged interface for this window matches that for the overall microstructure quite well. Windows containing 100 or less number of fibers exhibit regions with a deviation of 6% or more. Figure 10 depicts the change in the SERVE size for CIF distribution with the evolution of damage for all the loading cases. The largest microstructural windows of size 63  $\mu\text{m}$  containing 150 fibers is taken as the SERVE size required for characterizing the damaged microstructure from the distribution of CIF. The window of 63  $\mu\text{m}$  is independent of the loading direction, in the sense that it will satisfy the SERVE requirements for the three different boundary value problems considered. However, the SERVE window is not strictly location independent, due to the large SERVE size in comparison with the micrograph, resulting in overlapping regions.

## CONCLUSIONS

This paper extends the methodologies proposed in [2], to determine the statistically equivalent representative volume element (SERVE) for composite microstructures undergoing inclusion-matrix interfacial debonding. Interfacial debonding is accommodated in the Voronoi cell finite element model with the cohesive zone models. The cohesive parameters play an important role in the initiation and progression of debonding and hence the estimation of the RVE directly depends on the interface properties of the composite. The set of convergence measures for the SERVE including statistical functions, proposed in [2], are modified to provide meaningful quantitative representation in the presence of evolving microstructural damage. These measures include convergence of the damaged stiffness tensor in unloading, convergence of the marked correlation function of

averaged traction and convergence of the distribution of fraction of interface that are damaged and on the verge of debonding. The metrics are applied to a micrograph of a unidirectional fiber-reinforced composite to test the efficacy of the method. While interfacial debonding is considered as the damage mode in this study, other damage modes like matrix or particle cracking can be easily accommodated in the framework through appropriate adjustments in the damage critical variables for statistical functions.

With increasing applied macroscopic strain, the extent of damage in the microstructure increases, which in turn results in an increase in the SERVE size. For the simulations run in this article for three different loading directions, the SERVE size grows to  $63\ \mu\text{m}$ , containing about 150 fibers at the terminal values of applied strain. The SERVE size can also be a function of the interface parameters, since these govern the extent of damage progression. However, this study is not intended to investigate the dependence of the SERVE size of the cohesive parameters and hence, the results reported are for a specific set of cohesive parameters. The rate of increase in size of the SERVE with evolving damage is found to reduce with increased straining, perhaps due to the saturation of the damaged region with respect to the size of the microstructure. Additionally, the slope of the rate of increase depends on the nature of the loading. The rate is found to be very similar for normal loadings in orthogonal directions, but is considerably lower for shear loading. The lower rate in the latter case is due to a slower progress of micromechanical damage caused by the applied shear boundary conditions. This in turn may be attributed to a lesser contribution of the tangential displacement jump  $\delta_t$  towards the total displacement jump  $\delta$ , than the normal displacement jump  $\delta_n$  due to the factor  $\beta (= 0.707 < 1)$ . Since the sample micrograph considered in this study is small in comparison with the large SERVE size, the SERVE is not strictly independent of location, resulting in overlapping regions.

The continual increase in the SERVE size in the microstructure with evolving damage provide grounds for its restricted use in homogenization schemes [7,17] that utilize the representative volume elements for evaluating constitutive models at the continuum level. The breakdown of the SERVE leading to a consideration of detailed micromechanical models of the microstructure is gaining popularity with hierarchical and concurrent multiscale models [17].

## ACKNOWLEDGMENTS

This work has been partially supported by the Air Force Office of Scientific Research through grant No. F49620-98-1-01-93 (Program Director: Dr B. L. Lee) and by the Army Research Office through grant No. DAAD19-02-1-0428 (Program Director: Dr B. Lamattina). This sponsorship is gratefully acknowledged. Computer support by the Ohio Supercomputer Center through grant PAS813-2 is also gratefully acknowledged.

## REFERENCES

1. Li, S. and Ghosh, S. (2004). Debonding in Composite Microstructures with Morphological Variations, *International Journal of Comp. Meth.*, **1**: 121–149.
2. Swaminathan, Shriram, Ghosh, Somnath and Pagano, N.J. (submitted with this paper). Statistically Equivalent Representative Volume Elements for Unidirectional Composite Microstructures, Part I: Without Damage, *Jour. Comp. Materials* (submitted).

3. Carol, I., Rizzi, E. and Willam, K. (1994). A Unified Theory of Elastic Degradation and Damage based on a Loading Surface, *Int. Jour. of Solids and Structures*, **31**: 2835–2865.
4. Chaboche, J.L. (1981). Continuum Damage Mechanics, A Tool to Describe Phenomena before Crack Initiation, *Nuclear Engineering Design*, **64**: 233–247.
5. Chow, C.L. and Wang, J. (1987). An Anisotropic Theory of Elasticity for Continuum Damage Mechanics, *Int. Jour. of Fracture*, **20**: 381–390.
6. Cordebois, J.P. and Sidoroff, F. (1982). Anisotropic Damage in Elasticity and Plasticity, *Jour. De Mecanique Theorique Et Appliquee*, 45–60.
7. Raghavan, P. and Ghosh, S. A Continuum Damage Mechanics Model for Unidirectional Composites Undergoing Interfacial Debonding, *Mech. Mater.* (in press).
8. Ghosh, S., Ling, Y., Majumdar, B.S. and Kim, R. (2000). Interfacial Debonding in Multiple Fiber-reinforced Composites, *Mech. Mater.*, **32**: 561–591.
9. Moorthy, S. and Ghosh, S. (2000). Adaptivity and Convergence in the Voronoi Cell Finite Element Model for Analyzing Heterogeneous Materials, *Comp. Meth. Appl. Mech. Engng.*, **185**: 37–74.
10. Moorthy, S. and Ghosh, S. (1996). A Model for Analysis of Arbitrary Composite and Porous Microstructures with Voronoi Cell Finite Elements, *Int. Jour. Numer. Meth. Engng.*, **39**: 2363–2398.
11. Ghosh, S. and Mukhopadhyay, S.N. (1991). A Two Dimensional Automatic Mesh Generator for Finite Element Analysis of Random Composites, *Comp. Struct.*, **41**: 245–256.
12. Needleman, A. (1992). Micromechanical Modeling of Interfacial Decohesion, *Ultramicroscopy*, **40**: 203–214.
13. Chandra, N., Li, H., Seth, C. and Ghonem, H. (2002). Some Issues in the Application of Cohesive Zone Models for Metal Ceramic Interfaces, *Int. Jour. Solids Struct.*, **39**: 2827–2855.
14. Geubelle, P.H. (1995). Finite Deformation Effects in Homogeneous and Interfacial Fracture, *Int. Jour. Solids Struct.*, **32**: 1003–1016.
15. Camacho, G.T. and Ortiz, M. (1996). Computational Modeling of Impact Damage in Brittle Materials, *Int. Jour. Solids Struct.*, **33**: 2899–2938.
16. Ortiz, M. and Pandolfi, A. (1999). Finite-deformation Irreversible Cohesive Element for Three-dimensional Crack-propagation Analysis, *Int. Jour. Numer. Meth. Engng.*, **44**: 1267–1282.
17. Raghavan, P. and Ghosh, S. (2004). Adaptive Multi-Scale Computational Modeling of Composite Materials, *Comp. Model. Engng. Sci.*, **5**: 151–170.

PROOF ONLY